Exploring the complex magnetic phase diagram of Ce_2PdGe_3: A neutron powder diffraction and μSR study

A. Bhattacharyya,[1,2,*] C. Ritter,[3,†] D. T. Adroja,[1,2] F. C. Coomer,[1] and A. M. Strydom[2,4]

[1]*ISIS Facility, Rutherford Appleton Laboratory, Chilton, Didcot Oxon OX11 0QX, United Kingdom*

[2]*Highly Correlated Matter Research Group, Physics Department, University of Johannesburg, P.O. Box 524, Auckland Park 2006, South Africa*

[3]*Institut Laue Langevin, 6 rue Jules Horowitz, 38042 Grenoble, France*

[4]*Max Planck Institute CPfS, Nöthnitzerstrasse 40, 01187 Dresden, Germany*

(Received 4 December 2015; revised manuscript received 28 June 2016; published 15 July 2016)

The magnetic state of the tetragonal compound Ce_2PdGe_3, which crystallizes in the space group $P4_2/mmc$, a derivative of the α-$ThSi_2$ structure, has been investigated by magnetic susceptibility, heat capacity, muon spin relaxation (μSR), and neutron diffraction measurements. Heat capacity data indicate two separate magnetic phase transitions at $T_{N_1} = 10.7$ K and $T_{N_2} = 2.3$ K. The presence of bulk long-range magnetic order is confirmed by our μSR study below 11 K, where a drop of nearly 2/3 in the muon initial asymmetry and a sharp increase in the muon depolarization rate were observed. Neutron powder diffraction reveals that only one out of two Ce sites becomes magnetically ordered with magnetic propagation vector $\kappa = (0)$ at T_{N_1}, adopting an antiferromagnetic arrangement of magnetic moments $\mu_{Ce^{3+}} = 1.78(1)\mu_B$ along the c axis. At T_{N_2} the second Ce site orders similarly, following the same magnetic propagation vector $\kappa = (0)$, showing, however, at the same time a significant ferromagnetic component within the tetragonal basal plane. A second propagation vector, $\kappa = (\frac{1}{2},0,\frac{1}{2})$, appears concomitantly at T_{N_2}.

DOI: 10.1103/PhysRevB.94.014418

I. INTRODUCTION

The search for unusual physical phenomena in cerium, ytterbium, and uranium intermetallic compounds [1–6] features in the broader dome of strongly correlated electron systems for both experimentalists and theoreticians, as they provide an ultimate ground for exploring and testing new models to understand the complex phenomena such as spin glass behavior [7,8], Kondo effect [9], heavy fermions [10], unconventional superconductivity [11], intermediate valence state [12], and novel magnetism [13–15] shown by these systems. Numerous ground states were realized due to the competition between the Ruderman-Kittel-Kasuya-Yosida (RKKY) interaction and the Kondo interaction. Their study is important in order to understand the interplay between various order parameters involving spin and charge degrees of freedom, and their role in stabilizing new quantum phases of matter [16–20].

Novel ternary rare-earth intermetallic [21] compounds R_2TX_3 (R = rare-earth element, Ce, U; T = transition-metal element, Cr, Mn, Fe, Co, Ni, Cu, Rh, Pd, Pt, and Au; X = Si, Ge, Ga, In) represent a remarkable branch of this research field due to their complex and intriguing magnetic structures and physical properties, as, for example, multiple magnetic transitions, disordered magnetism, Kondo effect, and heavy fermion behavior. Most of the R_2TX_3 compounds crystallize in AlB_2-type or derived AlB_2-type structures, which is the important unit of numerous prototypical strongly correlated electron systems, which include $CaBe_2Ge_2$, $ThCr_2Si_2$, and $BaNiSn_2$ [22,23]. In R_2TX_3 the random sharing of crystallographic sites by T and X atoms produces a varying environment around the R ions and causes an alteration in the RKKY mediated exchange interaction, which will enable the formation of a spin glass. Ce_2NiGe_3 is a Kondo lattice system below room temperature where the electrical resistivity is attributable to the scattering from localized, unpaired cerium $4f$ electrons, i.e., magnetic resistivity increases as the temperature is lowered, instead of steadily decreasing, as is expected from the thermal scattering of conduction electrons by lattice vibrations [24]. Among the R_2TX_3 systems, there are many families categorized as R_2NiGe_3 [25], R_2PdSi_3 [26], R_2RhSi_3 [27], R_2AgIn_3 [28], and R_2CuIn_3 [29]. Each family typically presents various magnetic ground states with complicated magnetic structures originating from distinctive crystal structures. Mentioned here can be, e.g., the uranium-based compounds U_2MSi_3 [30], which show numerous unusual magnetic properties strongly related to the crystal structure of the sample where, e.g., for M = Pd, Pt, Au, Ir, and Rh, spin glass or cluster glass behavior is found [30].

Recently, Baumbach *et al.* [31] suggested that Ce_2PdGe_3 exhibits a Kondo-driven hybridization between the f-electrons and the conduction electron states. Their band structure calculations reveal a substantial f-electron weight close to the Fermi energy and the Sommerfeld coefficient of the heat capacity ($\gamma \approx 50$ mJ/mol Ce K^2) supports this point of view. Ce_2PdGe_3 forms in a tetragonal structure with space group $P4_2/mmc$, which is a derivative of the α-$ThSi_2$ type structure [22,23]. In this structure, cerium occupies two different sites ($2c$,$2f$) which have different local coordinations by Ge ($4g$) and Ge/Pd occupying the $4i$ site (Table I). The local symmetry of the Ce1 site ($\frac{1}{2},\frac{1}{2},0$) is "$mmm$" and Ce2 site ($\frac{1}{2},\frac{1}{4},\frac{1}{4}$) is "$-4m2$." The symmetry is lower than cubic and hence the Ce^{3+} $J = 5/2$ ground multiplet will split into three doublets for both of the Ce sites. In this paper we contribute a careful magnetic structure analysis in response to the need for this important information expressed in a previous work [31]. Our investigation on Ce_2PdGe_3 includes dc susceptibility [$\chi(T)$],

*amitava.bhattacharyya@stfc.ac.uk

†ritter@ill.fr

TABLE I. Results of the structural refinement in space group $P4_2/mmc$ of neutron diffraction data taken at room temperature with a neutron radiation of wavelength $\lambda = 1.05$ Å.

	z	B_{iso}	Occ.
Ce1 on $2c$	$z = 0$	0.60(2)	1
Ce2 on $2f$	$z = 0$	0.60(2)	1
Ge1/Pd on $4g$	0.3334(2)	0.76(2)	1
Ge2/Pd on $4i$	0.4170(1)	0.86(2)	0.53(4)/1.47(4)
R_{Bragg}	4.6		

isothermal magnetization (M), and heat capacity (C_P) data used for the magnetic characterization of the sample, muon spin relaxation (μSR), and very detailed neutron diffraction measurements. Below 11 K a sharp anomaly is observed in our $\chi(T)$ and $C_P(T)$ data which corresponds to a transition from the paramagnetic to an antiferromagnetic state. $C_P(T)$ data also show a second anomaly around 2.4 K. The presence of long-range magnetic order is also confirmed by μSR measurements where a two-thirds drop in the muon asymmetry is observed below 11 K. A doublet ground state is inferred from specific heat data. Neutron diffraction data show that the magnetic ground state is reached through a two-step, site-dependent magnetic ordering process and corresponds to a mainly antiferromagnetic arrangement of magnetic moments where, however, one of the two distinct Ce sites sees a significant ferromagnetic component. It is interesting to note that ferromagnetic ordering is rare in Ce-based compounds, which makes Ce_2PdGe_3 a member of a small group, which includes $CeRu_2Ge_2$ [32], $CeRh_3B_2$ [33], $CeRu_2M_2X$ (M = Al, Ga and X = B, C) [31,34], CeTX [35], and CeRuPO [36].

II. EXPERIMENTAL DETAILS

Polycrystalline samples of Ce_2PdGe_3 and La_2PdGe_3 were prepared by arc melting of the constituent elements (Ce: 99.999 wt. %; La: 99.999 wt. %; Pd: 99.999 wt. %; Ge: 99.999 wt. %) in an argon atmosphere on a water cooled copper hearth. Subsequently being flipped and remelted a number of times, the buttons were enfolded in tantalum foil and annealed at 850 °C for 168 h under a dynamic vacuum, better than 10^{-6} Torr. Powder x-ray diffraction measurements were carried out by means of a Panalytical X-Pert Pro diffractometer. Magnetization measurements were carried out using a Quantum Design magnetic property measurement system at temperatures between 2 and 300 K under an applied magnetic field of 1 kOe and for $0 < H < 70$ kOe at several different T. Temperature and field dependencies of the specific heat measurements were performed by the relaxation method in a Quantum Design physical property measurement system (PPMS).

Neutron diffraction measurements were carried out at the Institut Laue Langevin, Grenoble, France, using the high intensity D20 and the high resolution D2B powder diffractometers, using constant wavelengths of 2.41 and 1.05 Å, respectively. The powder sample was mounted in a 10 mm diameter vanadium can, which was cooled down to 2 K using a standard ^{4}He cryostat. The program FULLPROF [37] was used for Rietveld refinements and a magnetic symmetry analysis was performed using the program BASIREPS [38,39].

The muon spin relaxation experiment was carried out at the ISIS Pulsed Neutron and Muon Facility of the Rutherford Appleton Laboratory, United Kingdom. The μSR measurements were carried out on the EMU spectrometer with the detectors in a longitudinal configuration. The powdered sample was mounted onto a 99.995+% pure silver plate using diluted GE varnish and covered with kapton film which was cooled down to 1.2 K in a standard ^{4}He cryostat with He-exchange gas. At the ISIS facility, a pulse of muons is produced every 20 ms and has a full width of half maximum (FWHM) of $\approx$ 70 ns. These muons are implanted into the sample and decay with a half-life of 2.2 μs into a positron which is emitted preferentially in the direction of the muon spin axis. These positrons are detected and time stamped in the detectors which are positioned before, F, and after, B, the sample. The positron counts, $N_{F,B}(t)$, have the functional form

$$N_{F,B}(t) = N_{F,B}(0)e^{-t/\tau_\mu}[1 \pm G_z(t)], \quad (1)$$

where $G_z(t)$ is the longitudinal relaxation function. $G_z(t)$ is determined using

$$G_z(t) = [N_F(t) - \alpha N_B(t)]/[N_F(t) + \alpha N_B(t)], \quad (2)$$

where α is a calibration constant which was determined at 20 K by applying a small transverse magnetic field ($\approx$ 20 Oe) and adjusting its value until the resulting damped cosine signal was oscillating around zero.

III. RESULTS AND DISCUSSION

A. Magnetization and heat capacity

The magnetic susceptibility ($\chi = M/H$, where H is the applied magnetic field) measured in a zero-field-cooled condition in $H = 1$ kOe is shown in Fig. 1(a). $\chi(T)$ shows a clear drop below 11.0 K and a weak anomaly near 3 K with decreasing temperature. The first temperature corresponds to the paramagnetic to antiferromagnetic (PM/AFM) transition (T_{N_1}) in the sample. A comprehensive discussion is given in our neutron diffraction part. The temperature dependence of the heat capacity at zero field of Ce_2PdGe_3 and La_2PdGe_3 from 1.85 to 300 K is shown in Fig. 1(b). For La_2PdGe_3, the $C_P(T)$ data are typical for a nonmagnetic metal. For Ce_2PdGe_3, anomalies are observed at $T_{N_1} = 11.0$ K and at $T_{N_2} = 2.3$ K, which match well with previous reports, although we cannot detect the additional shoulder seen in Ref. [31] at about 11 K. The shift of the low temperature peak positioned in the zero-field heat capacity data at 2.3 K to higher temperatures in applied fields [Fig. 1(c)] suggests that Ce_2PdGe_3 in its low T phase is ferromagnetic. We note that it is a rare occurrence for Kondo screened cerium compounds to order ferromagnetically, as the Kondo effect is construed from an antiferromagnetic exchange between the local moment and the conduction electron screening cloud. On the other hand, the high temperature peak broadens with applied magnetic fields, suggesting the presence of an antiferromagnetic state. As shown in Fig. 1(d), the effect of crystal electric field is reflected as a broad Schottky-type anomaly centered around 50 K in C_{mag}. The solid curve in Fig. 1(d) represents the crystal field contribution to specific heat according to the crystal electric field (CEF) level scheme obtained from the analysis of our unpublished inelastic neutron scattering data

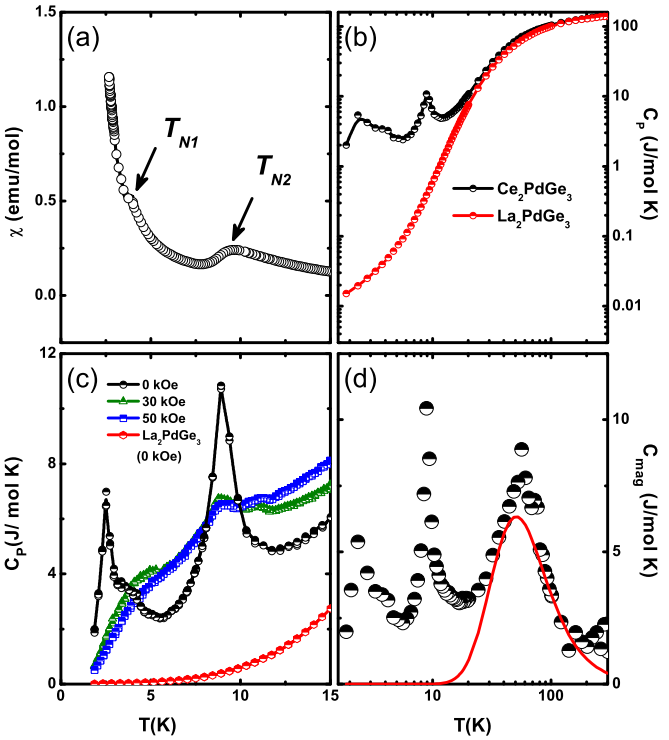

FIG. 1. (a) Temperature dependence of the dc magnetic susceptibility [$\chi(T)$] of polycrystalline Ce_2PdGe_3. (b) Temperature dependence of the specific heat of Ce_2PdGe_3 (black) and the phonon reference compound La_2PdGe_3 (red). (c) Low temperature specific heat in the presence of applied magnetic field $H = 0$, 30, and 50 kOe. (d) The temperature dependence of the estimated magnetic contribution of the heat capacity. The solid line shows the calculated heat capacity using the crystal field Schottky contribution (see text).

[40]. As there are two Ce sites, we find four CEF transitions from the ground state at 13.05 and 21.45 meV for the first Ce1 site and 16.05 and 28.25 meV for the second Ce2 site.

B. Muon spin relaxation

In order to shed light on the complex magnetic phase transitions seen in the zero-field heat capacity of Ce_2PdGe_3 below 11 K, we have investigated the temperature dependence of the muon spin relaxation in zero field. Spectra showing the time dependence of the muon decay asymmetry with fits of Ce_2PdGe_3 measured at various temperatures in zero field are shown in Fig. 2(a). The μSR spectra exhibit a typical behavior expected from the fluctuating paramagnetic moments with a full initial asymmetry of 20% at 20 K. Below 11 K a loss in the initial asymmetry is clearly seen, which is confirmation of long-range magnetic ordering. Below 11 K, as shown in Fig. 2(a), muon spin precession is not observable due to the fact that internal fields exceed the maximum internal field detectable on the EMU spectrometer due to the finite pulse width of the ISIS muon beam. The zero-field μSR spectra were fitted using an exponential decay function,

$$G_z(t) = A_1 \exp(-\lambda t) + A_{\rm bg}, \qquad (3)$$

where A_1 is the initial asymmetry parameter, λ is the electronic relaxation rate mainly arising from the local moments, and $A_{\rm bg}$ is a nonrelaxing constant background from the silver sample

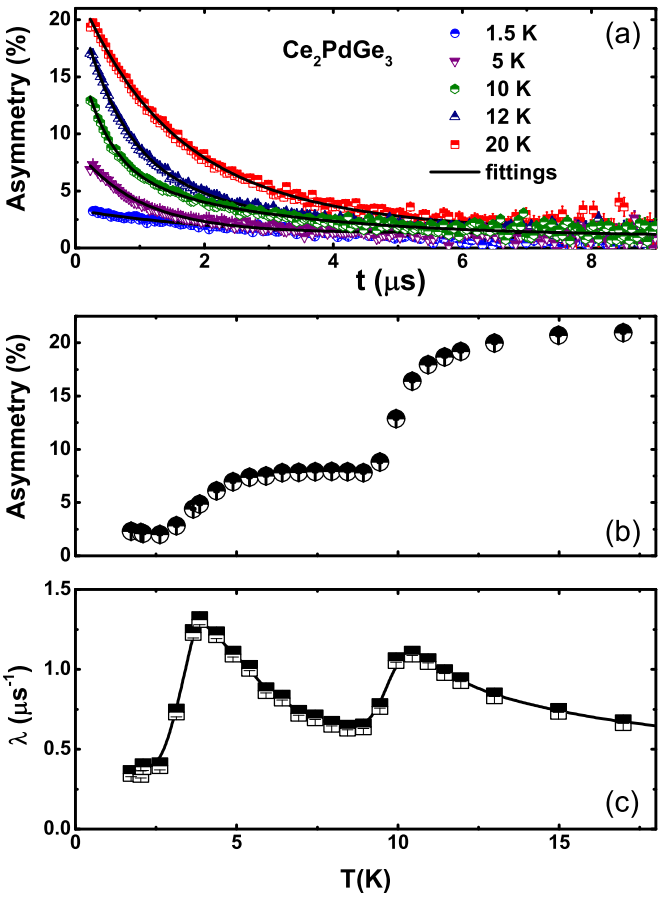

FIG. 2. (a) Zero-field μSR spectra plotted as asymmetry vs time at various temperatures of Ce_2PdGe_3. The solid lines depict fits using Eq. (3) [see text; $G_z(t) = A_1 \exp(-\lambda t) + A_{\rm bg}$]. Temperature T dependence of (b) the initial asymmetry A_1 and (c) the depolarization rate λ obtained from the analysis of the zero-field μSR data of Ce_2PdGe_3 for $1.2 \leqslant T \leqslant 20$ K. [The data presented in (a) are binned to improve the presentation and hence near $t = 0$ it will show more effects of binning on the initial asymmetry. Fit parameters obtained in (b) and (c) are obtained from the raw data.]

holder. $A_{\rm bg}$ was estimated from the 20 K zero-field (ZF) data and was kept fixed for the rest of the analysis.

The temperature dependencies of these parameters are shown in Figs. 2(b) and 2(c). At 11 K, as shown in Fig. 2(b), there is a loss of 2/3 of the value of the initial asymmetry (1/3 is left) A_1 from the high temperature value, indicating the presence of a long-range ordered state in the full volume of Ce_2PdGe_3, which agrees with the specific heat, magnetic susceptibility, and neutron diffraction data. The temperature dependence of the exponential decay term is shown in Fig. 2(c). The muon depolarization rate (λ) increases at T_{N_1}, indicating a transition between the paramagnetic and the ordered states. A second anomaly in λ as well as in the asymmetry is visible at T_{N_2}, where the second Ce site orders magnetically, as will be shown in the detailed discussion of the neutron results below.

C. Neutron diffraction

The high resolution neutron diffraction data taken at room temperature confirm the tetragonal structure of Ce_2PdGe_3 as described before by Baumbach *et al.* [31]. The refinement of

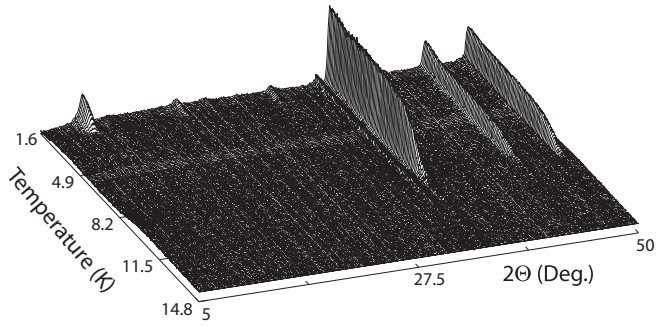

FIG. 3. Temperature dependence of the magnetic scattering of Ce_2PdGe_3 below 15 K. Plot created by subtracting a data set measured at 15 K, which is in the paramagnetic region.

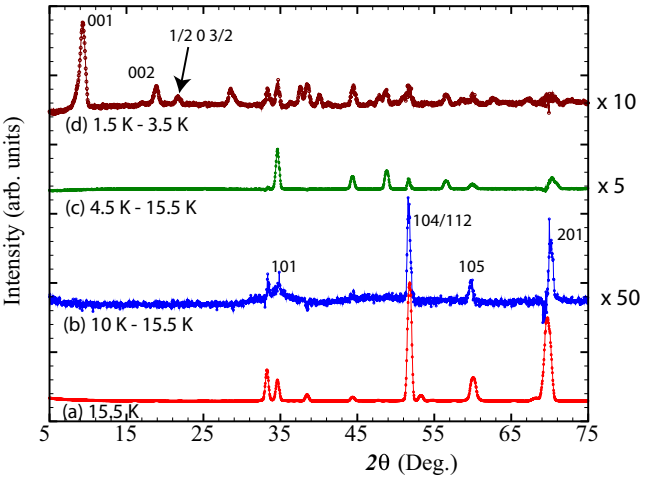

FIG. 4. Diffraction data of Ce_2PdGe_3 characteristic for the three different low temperature regions: (a) Purely nuclear scattering at 15 K of the paramagnetic phase. (b) Difference pattern 10–15 K showing weak short-range magnetic scattering at the position of the (101) reflection and a small increase of some high angle reflections; a multiplying factor of 50 was applied. (c) Difference pattern 4.5–15.5 K characteristic of the $\kappa = (0)$ type magnetic structure of the Ce2 sublattice plotted with a multiplying factor of 5. (d) Difference pattern 1.5–3.5 K multiplied by a factor of 10 showing magnetic peaks created mainly through the magnetic order with $\kappa = (0)$ of the Ce1 sublattice and those following the second magnetic propagation vector $\kappa = (\frac{1}{2},0,\frac{1}{2})$.

the occupation of the $4i$ site shared by palladium and germanium atoms determines a stoichiometry of $Ce_2Pd_{1.47}Ge_{2.53}$ for our compound [41]. Table I contains the information on the structural details. The thermal dependence of the high intensity neutron diffraction spectra reveals an increase in the intensity of several Bragg peaks below about 10 K and the appearance of additional Bragg reflections below about 3 K. As the changes are relatively small, a data set measured above the transitions at 15 K has been subtracted from all spectra in order to create the difference thermodiffractogram (Fig. 3), which displays the low 2Θ angle region where the magnetic scattering is the most intense.

Difference spectra created from the longer scans having better statistics reveal very small changes to be already present at 11.5 K. Using our prior knowledge from the single crystal study [31], it is therefore possible to define three different low temperature regions for Ce_2PdGe_3 (Fig. 4): The first region extends between 11.5 and 10 K where a broad, short-range-order-like intensity increases at the position of the (101) peak and an increase of three, relatively high angle peaks [(104/112), (105), (201)] are just detectable. The second region extends between 9.5 and 3.5 K and sees a now much stronger intensity increase at the position of allowed nuclear Bragg reflections. The third region starts below 3.5 K and is characterized by the appearance of several new Bragg reflections at positions not allowed by the nuclear symmetry $P4_2/mmc$.

Comparing these findings to the available macroscopic results, it can be said that while the transition to the first region has only been detected in the heat capacity data reported in Ref. [31], the transitions to the second and third region correspond nicely to the anomalies seen in the magnetic and muon spectroscopy data.

As the main intensity changes in the neutron diffraction data at the first transition appear at relatively high Q values, the magnetic origin of this transition can be questioned as the intensity of magnetic Bragg reflections will decrease as a function of the square of the magnetic form factor of Ce^{3+}. Indexing the corresponding Bragg reflections, a magnetic propagation vector $\kappa = (0)$ is found for this hypothetical magnetic structure. By applying a magnetic symmetry analysis using the program BASIREPS [38,39], the allowed irreducible representations (IRs) and their basis vectors (BVs) were determined for the two different Wykoff sites $2c$ and $2f$ where the Ce ions are placed (Table II). All possible combinations of the IRs and their BVs were tested, but none of the allowed magnetic structures are able to produce the intensity changes found in region 1 for the Bragg reflections [42].

In order to verify whether the small additional intensity found below 11.5 K on the nuclear reflections could be related to a structural change, additional high resolution diffraction data were collected at 20 and 10.5 K, however, no change of any structural parameter was found. We therefore attribute this first transition at 11.5 K to the appearance of magnetic

TABLE II. Basis vectors (BVs) of the allowed irreducible representations (IRs) for $\kappa = (0)$ for the Wyckoff positions $2c$ and $2f$ of space group $P4_2/mmc$

$\kappa = 0$	BV$_1$	BV$_2$	BV$_3$	BV$_4$	BV$_1$	BV$_2$
$2c$					$2f$	
IR1						
x,y,z	0 0 1				0 0 1	
$y,x,-z+\frac{1}{2}$	0 0 −1				0 0 −1	
IR2						
x,y,z	0 0 1				0 0 1	
$y,x,-z+\frac{1}{2}$	0 0 1				0 0 1	
IR3						
x,y,z	0 1 0	0 0 0	0 0 0	1 0 0	1 0 0	0 1 0
$y,x,-z+\frac{1}{2}$	0 0 0	0 1 0	1 0 0	0 0 0	−1 0 0	0 −1 0
IR4						
x,y,z					0 1 0	1 0 0
$y,x,-z+\frac{1}{2}$					0 1 0	1 0 0

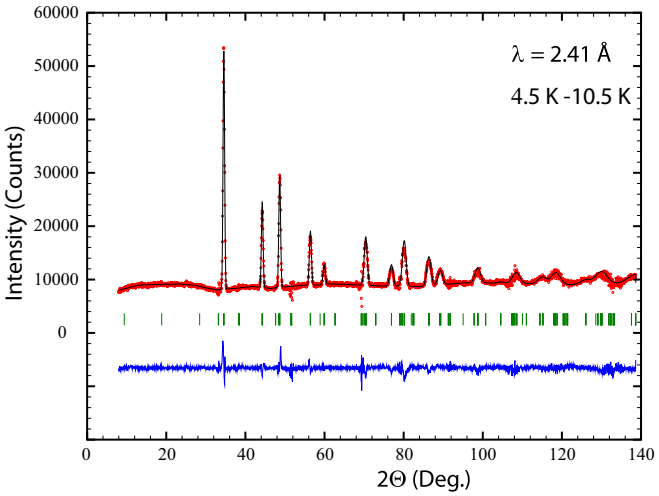

FIG. 5. Rietveld refinement of the difference pattern 4.5–10.5 K. Observed (dots, red), calculated (line, black), and difference pattern (line, blue). The tick marks indicate the calculated position of the magnetic peaks.

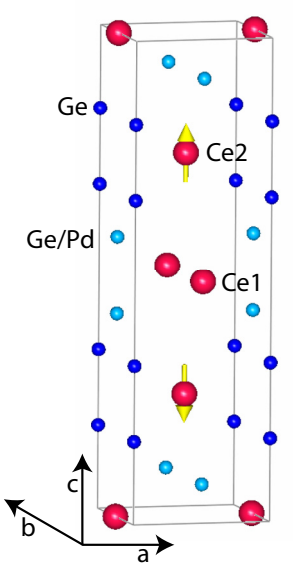

FIG. 6. Magnetic structure of Ce_2PdGe_3 between 3 and 10 K with $\kappa = (0)$.

short-range order and the slight changes in the intensities of some nuclear reflections tentatively to a type of extinction effect.

The magnetic peaks appearing below 10 K [Fig. 4 (c)] are indexed with the magnetic propagation vector $\kappa = (0)$. Using again the information from the symmetry analysis (Table II), the magnetic structure can be refined using IR1 of the Ce2 placed on the $2f$ site. There is no magnetic contribution in the diffraction pattern coming from the second cerium ion (Ce1 on Wyckoff site $2c$). The Rietveld refinement of the difference spectrum 4.5–10.5 K was made using the scale factor determined from the purely nuclear refinement of data taken at 15 K and is shown in Fig. 5. The magnetic structure corresponds to a simple antiferromagnetic arrangement of magnetic moments $\mu_{Ce^{3+}} = 1.78(1)\mu_B$ along the c axis with the spins oriented as well along the c direction (Fig. 6).

The new magnetic peaks appearing below 3 K are indexed with two different magnetic propagation vectors. While, e.g., the first two strong magnetic reflections at low angles can be indexed as (001) (9.4°) and (002) (18.8°) using the same $\kappa_1 = (0)$ already present below 10 K, other, newly appearing reflections are created through $\kappa_2 = (\frac{1}{2},0,\frac{1}{2})$. Fitting the intensity of the new magnetic peaks, it appears that—independent of the magnetic propagation vector they are created through—the magnetic transition is positioned at 2.6 K. The new magnetic peaks corresponding to $\kappa = 0$ are mainly created by the onset of magnetic ordering on the second cerium site (Ce1 on $2c$) which remained nonordered in the temperature range between 10 and 3 K. It orders antiferromagnetically with moments aligned in the direction of the c axis corresponding to IR1 of Ce1 (Table II). This order is identical to the interaction found already for the Ce2 site below 10 K. A second coupling—corresponding to IR3 of Ce1—however also becomes active below 2.6 K, which leads to a ferromagnetic component within the a-b plane on this Ce1 site. It is not possible due to the tetragonal structure of the compound to determine from powder data the direction of this ferromagnetic component within the basal plane. The transition below 3 K also affects the magnetic order on the Ce2 site: An antiferromagnetic coupling within the a-b plane corresponding to IR3 (Wyckoff position $2f$, right column of Table II) is established and adds itself to the antiferromagnetic order along the c axis (IR1) already existing below 10 K. It is this coupling within the a-b plane which creates, e.g., the low angle reflection (100) at $2\Theta = 9.4°$. Contrary to the Ce1 site, no ferromagnetic component exists on the Ce2 site.

As explained above, a second set of new magnetic peaks that appears below 10 K is created through a second magnetic propagation vector $\kappa = (\frac{1}{2},0,\frac{1}{2})$. Table III shows the corresponding allowed IRs and their BVs for the two different Ce sites. It can be seen that there are no longer any symmetry constraints for the Ce1 site on the Wyckoff position $2c$ as the site gets split into two independent orbits. The Ce2 site on the Wyckoff position $2f$ has IRs allowing ferro- or antiferromagnetic order in any of the three orthogonal directions between the two symmetry related $(x,y,z$ and $x,y,-z)$ atoms. Testing the different allowed possibilities, it is found that the magnetic peaks created through the $\kappa = (\frac{1}{2},0,\frac{1}{2})$ propagation vector can be refined assuming an antiferromagnetic order within the tetragonal basal plane. It is not possible to decide whether it is the Ce1 or the Ce2 site which is ordering (for the Ce2 site this antiferromagnetic order corresponds to IR2 or IR4 of Table III) as both solutions give equivalent refinements. Assuming that both sites contribute to the $\kappa = (\frac{1}{2},0,\frac{1}{2})$ phase, no stable refinement is possible. The moment size of this magnetic component amounts to about $0.71(1)\mu_B$ with spins lying in the a-b plane.

Table IV collects the results of the refinements of the magnetic structures at low temperatures and gives the individual moment components on the two Ce sites for both solutions. Figure 7 displays the magnetic structure for the solution where the Ce2 site possesses the additional $\kappa = (\frac{1}{2},0,\frac{1}{2})$ contribution,

TABLE III. Basis vectors (BVs) of the allowed irreducible representations (IRs) for $\kappa = (\frac{1}{2},0,\frac{1}{2})$ for the Wyckoff positions $2c$ and $2f$ of space group $P4_2/mmc$. The site $2c$ gets split into two independent orbits under the action of the magnetic propagation vector; $x,y,z = 0,\frac{1}{2},0$ and $\frac{1}{2},0,\frac{1}{2}$.

$\kappa = (\frac{1}{2},0,\frac{1}{2})$	BV_1		BV_1
$2c$		$2f$	
IR1		IR1	
x,y,z	0 1 0	x,y,z	0 1 0
		$-x,y,-z$	0 1 0
IR2		IR2	
x,y,z	1 0 0	x,y,z	1 0 0
		$-x,y,-z$	−1 0 0
IR3		IR3	
x,y,z	0 0 1	x,y,z	1 0 0
		$-x,y,-z$	1 0 0
		IR4	
		x,y,z	0 1 0
		$-x,y,-z$	0 −1 0
		IR5	
		x,y,z	0 0 1
		$-x,y,-z$	0 0 −1
		IR6	
		x,y,z	0 0 1
		$-x,y,-z$	0 0 1

and Fig. 8 the corresponding Rietveld refinement of the difference pattern 1.5–10.5 K.

IV. CONCLUSIONS

The complex magnetism and the strong electronic correlations in Ce_2PdGe_3 which crystallizes in the space group $P4_2/mmc$, a derivative of the α-$ThSi_2$ structure, have been studied using magnetic susceptibility, heat capacity, and microscopic tools of μSR and neutron powder diffraction. A complicated magnetic behavior with the presence of two magnetic transitions was detected and linked to the existence of two Ce sites in the crystal structure. The μSR data confirm the bulk nature of the long-range magnetic ordering below 11 K. Neutron diffraction reveals antiferromagnetic order

TABLE IV. Results of the refinement of the low temperature magnetic structure. Antiferromagnetic (AF) and ferromagnetic (F) components of the two magnetic propagation vectors on the two Ce sites. All components and the total resulting magnetic moment values μ_{Ce} in μ_B.

$\kappa = 0$	AF $\|\|c$	F $\perp c$	AF $\perp c$	$\kappa = (\frac{1}{2}0\frac{1}{2})$	AF $\perp c$
Ce1($2c$)	0.69(2)	0.63(1)			0.71(1)
Ce2($2f$)	1.69(1)		0.74(1)	0.71(1)	
R_{mag}		7.9		16.0	15.9
μ_{Ce}	0.93[a]	1.17[b]	Ce1($2c$)		
μ_{Ce}	1.98[a]	1.84[b]	Ce2($2f$)		

[a] $\kappa = (\frac{1}{2},0,\frac{1}{2})$ only acting on Ce2.
[b] Only acting on Ce1.

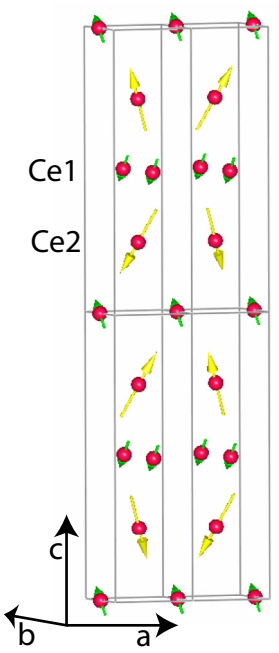

FIG. 7. Magnetic structure of Ce_2PdGe_3 at the base temperature assuming that the $\kappa = (\frac{1}{2},0,\frac{1}{2})$ contribution embraces the Ce2 sublattice. Short arrows represent magnetic spins on the Ce1 sublattice, and long arrows those on the Ce2 sublattice.

below $T_{N_1} = 11$ K and ferromagneticlike behavior below $T_{N_2} = 2.5$ K. At T_{N_1} only one out of two Ce sites becomes magnetically ordered, adopting an antiferromagnetic arrangement of magnetic moments $\mu_{Ce^{3+}} = 1.78(1)\mu_B$ along the c axis. At T_{N_2} the second Ce site orders similarly, following the same magnetic propagation vector $\kappa = (0)$, showing, however, at the same time, a significant ferromagnetic component within the tetragonal basal plane. A second propagation vector, $\kappa = (\frac{1}{2},0,\frac{1}{2})$, appears concomitantly at T_{N_2}. Inelastic neutron scattering experiments are in progress by our group [40] to determine the antiferromagnetic and ferromagnetic spin wave energy scale and the information on the crystal field splitting scheme.

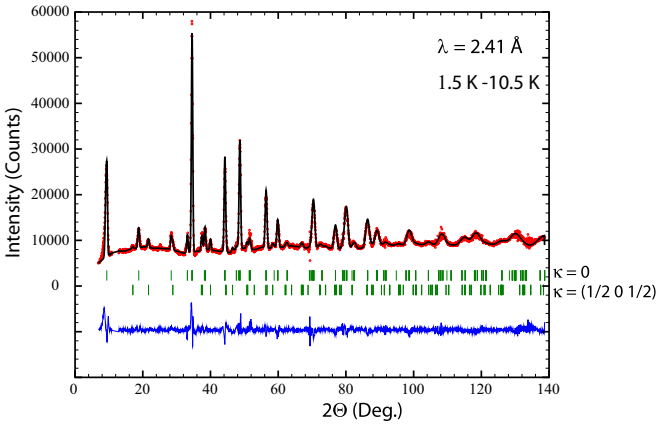

FIG. 8. Rietveld refinement of the difference pattern 1.5–10.5 K. Observed (dots, red), calculated (line, black), and difference pattern (line, blue). The tick marks indicate the calculated position of the magnetic peaks [upper row for $\kappa = (0)$, lower row for $\kappa = (\frac{1}{2},0,\frac{1}{2})$].

ACKNOWLEDGMENTS

We would like to thank A. D. Hillier for an interesting discussion on the μSR results. A.B.would like to acknowledge SA-NRF, FRC of UJ, ISIS-STFC and DST, India for funding support. D.T.A. would like to thank CMPC-STFC, Grant No. CMPC-09108, for financial support. A.M.S. thanks the SA-NRF (Grant No. 93549)and UJ Research Committee for financial support. D.T.A. would like to thank JSPS for funding and Professor Toshiro Takabatake for his kind hospitality at Hiroshima University.

[1] A. Georges, G. Kotliar, W. Krauth, and M. J. Rozenberg, Rev. Mod. Phys. **68**, 13 (1996).
[2] C. M. Varma, Rev. Mod. Phys. **48**, 219 (1976).
[3] P. Coleman, in *Handbook of Magnetism and Advanced Magnetic Materials*, edited by H. Knoemuller and S. Parkin (Wiley, New York, 2007), Vol. 1, p. 95.
[4] P. S. Riseborough, Adv. Phys. **49**, 257 (2000); Phys. Rev. B **45**, 13984 (1992).
[5] G. R. Stewart, Rev. Mod. Phys. **73**, 797 (2001); A. Amato, *ibid.* **69**, 1119 (1997).
[6] H. v. Löhneysen, A. Rosch, M. Vojta, and P. Woelfle, Rev. Mod. Phys. **79**, 1015 (2007).
[7] N. Marcano, A. Senas, J. I. Espeso, L. F. Barquin, J. R. Fernandez, and J. C. G. Sal, J. Non-Cryst. Solids **287**, 318 (2001).
[8] R. Mallik, E. V. Sampathkumaran, M. Strecker, G. Wortmann, P. L. Paulose, and Y. Ueda, J. Magn. Magn. Mater. **185**, L135 (1998).
[9] E. Borchi and S. D. Gennaro, Phys. Rev. B **14**, 1989 (1975).
[10] Y. Hirose, N. Nishimura, F. Honda, K. Sugiyama, M. Hagiwara, K. Kindo, T. Takeuchi, E. Yamamoto, Y. Haga, M. Matsuura, K. Hirota, A. Yasui, H. Yamagami, R. Settai, and Y. Onuki, J. Phys. Soc. Jpn. **80**, 024711 (2011).
[11] O. Stockert, J. Arndt, E. Faulhaber, C. Geibel, H. S. Jeevan, S. Kirchner, M. Loewenhaupt, K. Schmalzl, W. Schmidt, Q. Si, and F. Steglich, Nat. Phys. **7**, 119 (2011).
[12] K. A. Gschneidner and V. K. Pecharsky, Physica B **223**, 131 (1996).
[13] J. D. Thompson, T. Park, N. J. Curro, F. Ronning, R. Movshovich, E. D. Bauer, and J. L. Sarrao, J. Magn. Magn. Mater. **310**, 532 (2007).
[14] N. Kumar, P. K. Das, R. Kulkarni, A. Thamizhavel, S. K. Dhar, and P. Bonville, J. Phys.: Condens. Matter **24**, 036005 (2012).
[15] S. Majumdar and E. V. Sampathkumaran, Solid State Commun. **117**, 645 (2001).
[16] S. Doniach, Physica B+C **91**, 231 (1977).
[17] J. Kondo, Prog. Theor. Phys. **32**, 37 (1964).
[18] M. A. Ruderman and C. Kittel, Phys. Rev. **96**, 99 (1954).
[19] T. Kasuya, Prog. Theor. Phys. **16**, 45 (1956).
[20] K. Yosida, Phys. Rev. **106**, 893 (1957).
[21] P. Z. Yan, C. C. De, B. X. Jun, S. R. Bo, Z. J. Bang, and D. L. Bing, Chin. Phys. B **22**, 056102 (2013).
[22] E. Parthe, B. Chabot, H. F. Braun, and N. Engel, Acta Crystallogr., Sect. B **39**, 588 (1983).
[23] W. B. Pearson, J. Solid State Chem. **56**, 278 (1985).
[24] D. Huo, J. Sakurai, T. Kuwai, Y. Isikawa, and Q. Lu, Phys. Rev. B **64**, 224405 (2001).
[25] J. W. Chen, Y. S. Guan, and C. H. Wang, J. Phys.: Conf. Ser. **266**, 012006 (2010).
[26] M. Frontzek, A. Kreyssig, M. Doerr, M. Rotter, G. Behr, W. Loser, I. Mazilu, and M. Loewenhaupt, J. Magn. Magn. Mater. **301**, 398 (2006).
[27] W. Baela, B. Penc, N. Stüsser, A. Szytua, E. Wawrzyska, and A. Zygmunt, Physica B **350**, E167 (2004).
[28] J. Siouris, J. P. Semitelou, J. K. Yakinthos, and W. Schäfer, Physica B **276**, 582 (2000).
[29] A. Szytua, A. Arulraj, S. Baran, D. Kaczorowski, B. Penc, and N. Stüsser, Solid State Commun. **147**, 61 (2008).
[30] R. Pöttgen, J. Alloys Compd. **201**, 157 (1993).
[31] R. E. Baumbach, A. Gallagher, T. Besara, J. Sun, T. Siegrist, D. J. Singh, J. D. Thompson, F. Ronning, and E. D. Bauer, Phys. Rev. B **91**, 035102 (2015).
[32] H. Wilhelm, K. Alami-Yadri, B. Revaz, and D. Jaccard, Phys. Rev. B **59**, 3651 (1999).
[33] A. L. Cornelius and J. S. Schilling, Phys. Rev. B **49**, 3955 (1994).
[34] E. Matsuoka, Y. Tomiyama, H. Sugawara, T. Sakurai, and H. Ohta, J. Phys. Soc. Jpn. **81**, 043704 (2012).
[35] B. M. Sondezi-Mhlungu, D. T. Adroja, A. M. Strydom, S.Paschen, and E. A. Goremychkin, Physica B **404**, 3032 (2009); S. K. Malik and D. T. Adroja, Phys. Rev. B **43**, 6295(R) (1991).
[36] C. Krellner, N. S. Kini, E. M. Bruning, K. Koch, H. Rosner, M. Nicklas, M. Baenitz, and C. Geibel, Phys. Rev. B **76**, 104418 (2007).
[37] J. Rodríguez-Carvajal, Physica B **192**, 55 (1993).
[38] J. Rodríguez-Carvajal, BASIREPS: a program for calculating irreducible representations of space groups and basis functions for axial and polar vector properties. Part of the FULLPROF suite of programs, www.ill.eu/sites/fullprof/.
[39] C. Ritter, Solid State Phenom. **170**, 263 (2011).
[40] A. Bhattacharyya and D. T. Adroja (unpublished).
[41] A simulation of the neutron diffraction data assuming the ideal 2:1:3 stoichiometry leads to just a minor change of the R_{Bragg} factor from 4.6 to 5.0 showing the weak sensitivity of the refinement to the exact Pd/Ge ratio. At the same time a strong correlation between the Pd/Ge occupation of the site 4*i* and the thermal *B* factor of this site was found. Taking into account the starting weight of the constituents used for the synthesis and very small weight lost (2%–3%) after the final melting, as well as the absence of impurity phases, there is no reasonable explanation for an increase of the Pd content, as reflected in the refined stoichiometry. As macroscopic data taken on our sample agree with those of Ref. [31], we therefore assume that our sample conforms as well closely to the 2:1:3 stoichiometry.
[42] Magnetic models having basis vectors within the *a*-*b* plane lead to strong magnetic reflections at low angles: ferromagnetic models to the (002) reflection at about $2\Theta = 18.9^\circ$ and antiferromagnetic models to the (001) reflection at about 9.4°. Spin arrangements where the magnetic moments point along the *c* axis create strong (100)(33.2°) and (011)(34.6°) reflections for ferromagnetic or strong (102)(38.4°), (013)(44.3°), and (111)(48.7°) reflections for antiferromagnetic models. All these reflections are absent or show a much weaker intensity increase compared to that of the high angle reflections [see Fig. 4(b)] which were used to define region 1.